A Robust In-Situ Warp-Correction Algorithm For VISAR Streak Camera Datat at the National Ignition Facility

G. Labaria, A. L. Warrick, P. M. Celliers, D. H. Kalantar

January 13, 2015

Disclaimer

This document was prepared as an account of work sponsored by an agency of the United States government. Neither the United States government nor Lawrence Livermore National Security, LLC, nor any of their employees makes any warranty, expressed or implied, or assumes any legal liability or responsibility for the accuracy, completeness, or usefulness of any information, apparatus, product, or process disclosed, or represents that its use would not infringe privately owned rights. Reference herein to any specific commercial product, process, or service by trade name, trademark, manufacturer, or otherwise does not necessarily constitute or imply its endorsement, recommendation, or favoring by the United States government or Lawrence Livermore National Security, LLC. The views and opinions of authors expressed herein do not necessarily state or reflect those of the United States government or Lawrence Livermore National Security, LLC, and shall not be used for advertising or product endorsement purposes.

A robust in-situ warp-correction algorithm for VISAR streak camera data at the National Ignition Facility

George R. Labaria[a,b], Abbie L. Warrick[b], Peter M. Celliers[b], and Daniel H. Kalantar[b]

[a]University of California, Santa Cruz, California, USA;
[b]Lawrence Livermore National Laboratory, Livermore, California, USA

ABSTRACT

The National Ignition Facility (NIF) at the Lawrence Livermore National Laboratory is a 192-beam pulsed laser system for high energy density physics experiments. Sophisticated diagnostics have been designed around key performance metrics to achieve ignition. The Velocity Interferometer System for Any Reflector (VISAR) is the primary diagnostic for measuring the timing of shocks induced into an ignition capsule. The VISAR system utilizes three streak cameras; these streak cameras are inherently nonlinear and require warp corrections to remove these nonlinear effects. A detailed calibration procedure has been developed with National Security Technologies (NSTec) and applied to the camera correction analysis in production. However, the camera nonlinearities drift over time affecting the performance of this method. An in-situ fiber array is used to inject a comb of pulses to generate a calibration correction in order to meet the timing accuracy requirements of VISAR. We develop a robust algorithm for the analysis of the comb calibration images to generate the warp correction that is then applied to the data images. Our algorithm utilizes the method of thin-plate splines (TPS) to model the complex nonlinear distortions in the streak camera data. In this paper, we focus on the theory and implementation of the TPS warp-correction algorithm for the use in a production environment.

Keywords: visar, streak camera, warp-correction, thin-plate splines

1. INTRODUCTION

The National Ignition Facility (NIF) at the Lawrence Livermore National Laboratory is a 192-beam pulsed laser system for high-energy density physics experiments. The NIF is the world's largest and most powerful laser system, and it is capable of creating high pressures, temperatures, and densities similar to those found during thermonuclear burn, in the cores of stars, and in supernovae. A primary goal of the NIF is to achieve ignition of a deuterium-tritium (DT) fuel capsule [1]. The NIF target is typically a gold hohlraum containing a DT fuel capsule. During a DT shot, NIF's 192 laser beams heat the hohlraum which converts the energy into x-rays. The x-rays heat the outer surface of the DT capsule, causing it to ablate and launch a series of shock waves into the capsule. These overlapping shock waves force the DT fuel layers inward, compressing it into a hotspot of extremely high temperature and density. Fusion reactions occur when the temperature and density are sufficiently high [2].

One of the key performance metrics for the optimization of the NIF's performance to achieve ignition is the timing of shocks induced into the DT capsule during a shot [2]. The Velocity Interferometry System for Any Reflector (VISAR) is used to infer the velocity of a moving surface by measuring its Doppler wavelength shift, and it is the primary optical diagnostic for measuring shock timing [3-4]. The VISAR diagnostic utilizes three streak cameras [5] to measure the Doppler wavelength shift. Streak cameras are inherently nonlinear, meaning that the streak camera's recordings in the space and time direction are displaced in a systematic nonlinear fashion, distorting the spatial and temporal measurements of the streak camera data [6].

To meet the timing accuracy requirements, the streak cameras in the VISAR system require warp corrections to remove the nonlinear effects. A detailed calibration procedure has been developed with National Securities
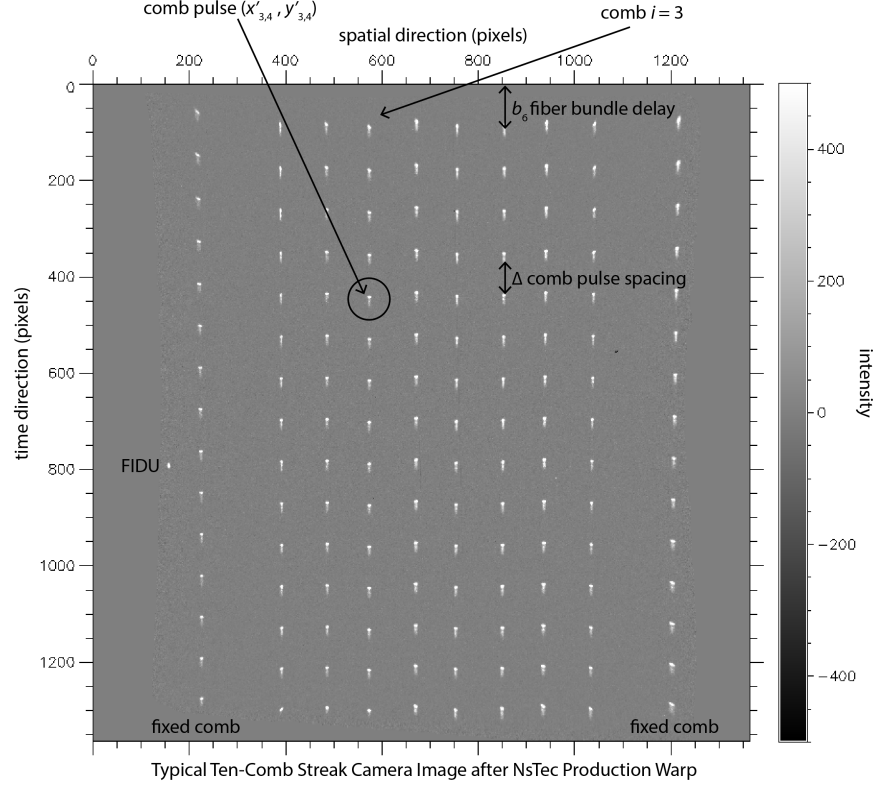

Figure 1. A typical ten-comb streak camera image after standard NSTec warp-corrections in production. The comb generator is split into ten different fibers. The two outer fibers are fixed, marking the boundary of the active spatial region. The remaining eight middle fibers can be retracted on demand before the full shot. The timing fiducial is shown, labeled FIDU and is represented by a single pulse.

Technologies (NSTec) and applied to the camera correction analysis in production [7]. However, the streak camera nonlinearities drift over time due to sweep rate jitter and slow thermal drift, negatively affecting the performance of this method. An additional warp correction is therefore required to meet the timing accuracy requirements of VISAR for key measurements [8]. To perform this additional correction, a multi-comb injection system is mounted outside the streak camera to generate a comb of pulses. Comb generators are available to produce frequencies of 0.5 GHz, 1 GHz, 3 GHz, or 10 GHz; the frequency is chosen to provide sufficient coverage of the sweep window. The output of the comb generator is split and delivered to the streak camera via ten different fibers. The resulting comb pulses cover the active spatial area and temporal sweep window which creates a two-dimensional grid from which the streak camera nonlinearities can be approximately characterized. Figure 1 shows a typical ten-comb streak camera image after the NSTec production warp. The comb pulse positions are calculated by a two-dimensional peak detection algorithm in production providing the (x, y)-coordinates of the comb pulses. This procedure provides data that allows for an in-situ calibration within minutes of a shot [8].

Thin-plate splines (TPS) are ideal for modeling complicated local distortions over irregularly sampled points, making it a good candidate for use as an in-situ warp-correction algorithm for VISAR. Before the TPS warp-correction algorithm can be applied, identification of the landmark points is required. The calculated comb pulse positions are used as the landmark points in our warp-correction map. The comb pulse data is preprocessed to improve the algorithms robustness by removing erroneous comb pulse positions reported by the peak-detection algorithm (see section 3.1). To prevent the image from resizing, an additional pre-processing step that identifies the boundary points in both the uncorrected and corrected image spaces is performed (see section 3.3). Once the landmark points from the comb pulses and boundaries are calculated, the warp-correction map is generated. A flowchart summarizing the main components of the warp-correction algorithm is given in figure 2. In this paper,
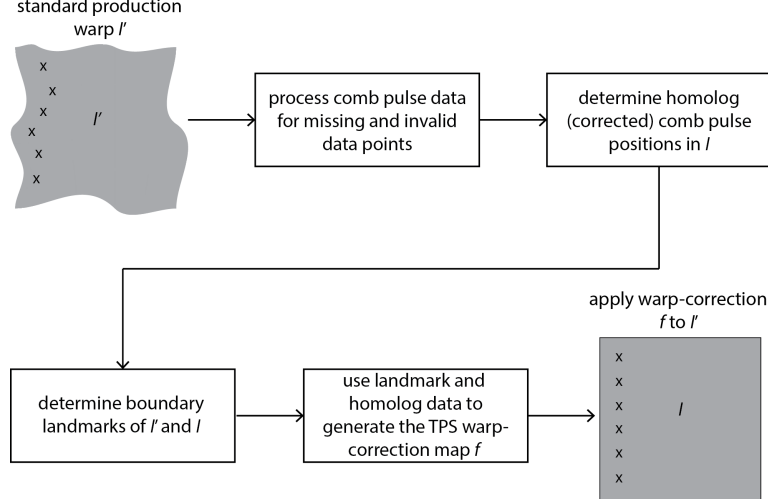
Figure 2. A flowchart summarizing the main components of the in-situ warp-correction algorithm. Each component will be explained in detail in section 3

a mathematical formalization for the TPS warp-correction algorithm is presented. Details required for a robust implementation in a production environment are then described. Finally, results for VISAR streak camera data are presented. The mathematical constructions written in this paper are self-contained assuming only a basic background in real analysis. For the reader not familiar with real analysis, necessary definitions are provided in section 7.

2. MATHEMATICAL PRELIMINARIES AND NOTATION

In this section, we present some mathematical notation and concepts that will be necessary for the development of the theory of the TPS warp-correction algorithm. Informally, we can consider the uncorrected image as an "irregularly shaped" region of $\mathbb{R}^2$. The corrected image is a square region in $\mathbb{R}^2$ of known length. The warp correction is a mapping that transforms the uncorrected image to the corrected image. The following discussion will make these notions more precise.

The TPS warp-correction algorithm performs an additional correction to the NSTec warp correction already in production. As mentioned in section 1, the streak camera nonlinearities drift over time, negatively impacting the performance of the NSTec warp correction. Throughout the rest of our paper, we will refer to the NSTec-corrected images as *uncorrected images*. The result of the TPS warp-correction algorithm when applied to those images will be referred to as the *corrected* images. We will always denote an uncorrected image by I' and a corrected image by I. Following this convention, points in the images will be denoted by (x', y') and (x, y) for points in I' and I respectively. We assume that I' is a closed, simply-connected subset of $\mathbb{R}^2$, and $I = [0, N-1] \times [0, N-1] \subset \mathbb{R}^2$ where N is the size of the corrected image*. Note that the precise shape of I' is unknown. We also assume that $\text{area}(I') = \text{area}(I)$; that is, the area of I' is the same as the area of I. The warp correction can be viewed as a mapping $f : \mathbb{R}^2 \to \mathbb{R}^2$ where $I' \xmapsto{f} I$. The mapping f is given by the method of thin-plate splines. One can show that f is continuous, smooth, and surjective [9]. If there is no folding (i.e., if f is injective), then f is bijective and hence is a diffeomorphism. Unfortunately for thin-plate splines, bijectivity is not guaranteed. Some characterizations of the restrictions necessary to ensure bijectivity are presented in [9], but this is still largely an open problem in mathematics. Bijective TPS maps are ideal since they preserve the topology of the image. As we will see in our application of the thin-plate splines, folding does not occur since parts of the corrected images are not smeared or folded onto each other. Thus to simplify the theory, we will assume that for the TPS warp-correction algorithm, the resulting map f is diffeomorphic. Figure 3 is a schematic illustration of the warp correction map on I'.

---

*the image size for the NIF VISAR is 1365×1365 pixels; so for our implementation, $N = 1365$.
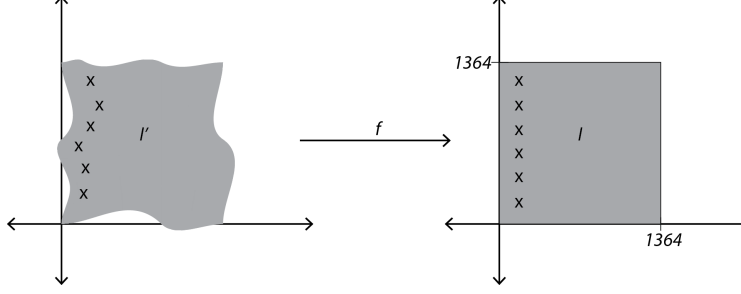
Figure 3. A schematic representation of the warp-correction map. The X's represent the landmark points and their homologs in the I' and I respectively. Note that the nonlinear distortion on I' is exaggerated for illustrative purposes; in practice, the nonlinear drifts are very small and difficult to see qualitatively.

2.1 Thin-Plate Splines

The method of thin-plate splines is a convenient tool to use for image warp corrections. They are ideal for modeling local nonlinear distortions that are difficult to model using polynomial-based interpolation techniques. The thin-plate spline has a very natural physical interpretation; it can be thought of like bending a thin sheet of metal in the vertical direction as a displacement of the x or y direction in a plane so that the metal sheet is least bent in the sense that its bending energy is minimized. In this subsection, we present the method of thin-plate splines more precisely. A beautiful introduction to thin-plate splines on $\mathbb{R}^2$ can be found in [10]. Duchon's original paper [11] and Meinguet's generalization [12] provide a more rigorous introduction.

Definition 1. Suppose we have a set of points $\{(x'_k, y'_k)\} \subset \mathbb{R}^2$ that we want to map to $\{(x_k, y_k)\} \subset \mathbb{R}^2$ such that $(x'_k, y'_k) \mapsto (x_k, y_k)$. We will refer to the points (x'_k, y'_k) as *landmark points* and their image (x_k, y_k) as their *homologs* or *corrected homologs*.

In the context of image warp-corrections, the landmark points are typically points in the image whose location we can measure. Since we can measure the comb pulse positions in the uncorrected image, we take those points to be our landmark points. To index the landmark points, let $(x'_{ij}, y'_{ij}) \in I'$ denote the coordinates of the comb pulse in the i-th comb and j-th pulse in comb i. As a convention, we start the index at 0. So for example, $(x'_{3,4}, y'_{3,4})$ is the comb pulse circled in figure 1. The corrected homolog points are indexed in the same way; for example, $(x_{3,4}, y_{3,4})$ is the homolog for the landmark point $(x'_{3,4}, y'_{3,4})$.

Definition 2. Suppose that there are n landmark points. A *thin-plate spline* on $\mathbb{R}^2$ is a vector-valued function $f : \mathbb{R}^2 \to \mathbb{R}^2$ defined by $(x, y) \mapsto (f_x(x, y), f_y(x, y))$ mapping each landmark point to its homolog in such a way that the resulting component surfaces f_x and f_y are least bent in the sense that the quadratic functional

$$I(f) = \int_{\mathbb{R}^2} \left[\left(\frac{\partial^2 f}{\partial x^2} \right)^2 + 2 \left(\frac{\partial^2 f}{\partial x \partial y} \right)^2 + \left(\frac{\partial^2 f}{\partial y^2} \right)^2 \right] dx dy, \tag{1}$$

is minimized over all such interpolating functions f_x and f_y. The component surfaces are of the form

$$f_x(x, y) = \underbrace{a_1 + a_2 x + a_3 y}_{\text{affine part}} + \underbrace{\sum_{k=1}^{n} w_k U \left(\|(x'_k, y'_k) - (x, y)\| \right)}_{\text{fully nonlinear part}}, \tag{2}$$

where $U(r) = r^2 \log r$, $r = \sqrt{x^2 + y^2}$, and $\|\cdot\|$ denotes the standard Euclidean metric. The y-component surface f_y is of a similar form.

Finding the coefficients for f_x and f_y so that the conditions in Definition 2 are satisfied requires solving a linear system which is presented in section 8. The resulting thin-plate spline map $f(x, y) = (f_x(x, y), f_y(x, y))$ satisfies the following properties:

1. $f(x'_k, y'_k) = (x_k, y_k)$ for all k.

2. The component functions f_x and f_y are least bent according to equation (1).

3. $f(x, y)$ is a diffeomorphism so long as there are no folds. This means that the restriction of f to the interior of I', $f|_{\text{int} I'} : \text{int} I' \to \text{int} I$ is a diffeomorphism so long as there are no folds.

4. The component functions f_x and f_y are the sum of an affine part and fully nonlinear part as given in equation (2). It can be shown that the fully nonlinear part is bounded and asymptotically flat, and the affine part describes the behavior at infinity. Thus, in the context of image warp corrections, the thin-plate spline method can be thought of as a local correction method; that is, the nonlinear corrections occur in a small neighborhood around the landmark points.

To see that fully nonlinear corrections occur around a small neighborhood of the landmark points, consider the example in figure 4. In this example, one landmark point is translated by $+1$ in the x-direction. In (a), two copies of $\mathbb{R}^2$ are shown. The left graph shows the landmark points $((1, 4), (4, 4), (1, 1), (4, 1))$ denoted by X's and the right graph shows the corresponding homolog points $((1, 4), (5, 4), (1, 1), (4, 1))$. All the landmark points are identically mapped to their homolog points with the exception of $(4, 4) \mapsto (5, 4)$. Since only the $(4, 4)$ landmark point is translated to $(5, 4)$, the thin-plate spline mapping is $f(x, y) = ((f_x(x, y), f_y(x, y)) = (f_x(x, y), y)$ where $f_x(x, y) = -0.5833 + 1.167x + 0.667y - 0.02U\left(\|(1, 4) - (x, y)\|\right) + 0.02U\left(\|(4, 4) - (x, y)\|\right) + 0.02U\left(\|(1, 1) - (x, y)\|\right) - 0.02U\left(\|(4, 1) - (x, y)\|\right)$, and $f_y(x, y) = y$ is the identity mapping in y since none of the landmark points are translated in the y-direction. Part (b) shows the fully nonlinear part of $f_x(x, y)$ (the linear combination of $U(x, y)$'s). The fully nonlinear part is asymptotically flat and bounded. This is seen more clearly in the next graph. In part (c), the full $f(x, y)$ is plotted. Although difficult to see, the fully nonlinear part only contributes to the surface in small neighborhoods around the landmark points. The rest of the surface is dominated by the affine part. This demonstrates that fully nonlinear warp corrections are only applied to a small neighborhood around the landmark points.

The TPS algorithm satisfies several requirements needed in a warp-correction algorithm. The next section discusses how the TPS warp correction can be made robust.

3. WARP-CORRECTION ALGORITHM DERIVATION

In this section, we explain in detail each module of our warp-correction algorithm shown schematically in figure 2.

3.1 Processing for Missing and Invalid Comb Pulse Data

The comb pulse (x, y)-positions in the uncorrected image I' (e.g. such as in figure 1) are given by a two-dimensional peak-detection algorithm in production. The detected comb pulses can be classified into three categories defined by the following definitions.

Definition 3. A comb pulse that is in I' but is not detected by the peak-detection algorithm is a *missing comb pulse*.

Definition 4. A comb pulse that is not in I' but is detected by the peak-detection algorithm is an *invalid comb pulse*.

Definition 5. A comb pulse that is in I' and is detected by the peak-detection algorithm is a *valid comb pulse*.

Suppose that there are m_i detected comb pulses in comb i, where $i = 0, \ldots, 9$. Enumerate the detected comb pulses by $\mathcal{P}' = \left\{ \left(x'_{ij_k}, y'_{ij_k} \right) \mid i = 0, \ldots, 9 \text{ and } j_k \in J_i \right\}$ where $J_i = \{j_k \mid k = 0, \ldots, m_i - 1 \text{ and } j_{k+1} > j_k\}$ is the detected comb pulse index set for comb i. Also, let $\mathcal{P}'_i$ denote the detected comb pulses in comb i, so that $\bigcup_{i=0}^9 \mathcal{P}'_i = \mathcal{P}'$. We assume that the streak camera nonlinearities result in small displacements. In particular, the y-coordinate of a detected comb pulse can be written as $y'_{ij_k} = b_i + \Delta j_k + \epsilon_{ij_k}$ where b_i is the fiber-bundle delay associated with comb i, Δ corresponds to the comb generator frequency, and $|\epsilon_{ij_k}|$ is small (see Figure 1). The quantity $|\epsilon_{ij_k}|$ is small in the sense that $|\epsilon_{ij_k}| << \Delta$; i.e., the nonlinear displacement in the y-direction is small relative to the comb pulse period.
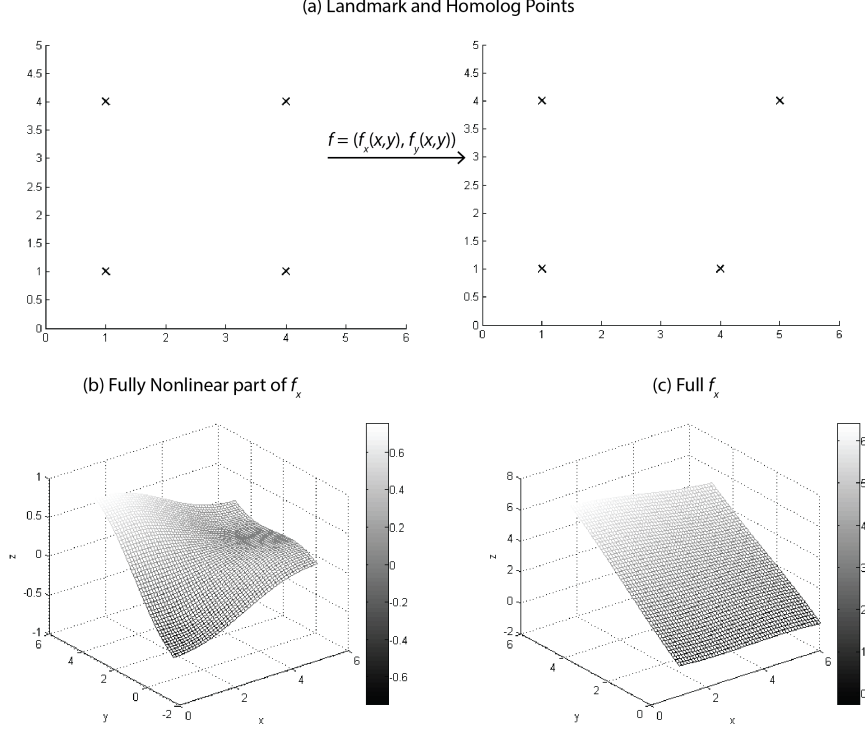
Figure 4. A simple example of a thin-plate spline mapping where one landmark point is translated by $+1$ in the x-direction demonstrating that the fully nonlinear warp-corrections are only applied to a small neighborhood around the landmark points.

We can further categorize the missing comb pulses: missing middle comb pulses and missing comb pulses at the end of a comb.

Definition 6. Consider a sequence of comb pulses $D = \left\{ \left(x'_{ij_1}, y'_{ij_1} \right), \ldots, \left(x'_{ij_k}, y'_{ij_k} \right) \mid y'_{ij_1} < \cdots < y'_{ij_k} \right\}$ in comb i in I' that are not detected by the peak-detection algorithm. If there are valid comb pulses $\left(x'_{ij_0^{(v)}}, y'_{ij_0^{(v)}} \right)$ and $\left(x'_{ij_1^{(v)}}, y'_{ij_1^{(v)}} \right)$ such that $y'_{ij_0^{(v)}} < y'_{ij_1}$ and $y'_{ij_k} < y'_{ij_1^{(v)}}$ in $\mathcal{P}'_i$, then the comb pulses in D are *missing middle comb pulses*.

Consider the difference between the y-coordinate of two successive comb pulses $\left(x'_{ij_k}, y'_{ij_k} \right)$ and $\left(x'_{ij_{k+1}}, y'_{ij_{k+1}} \right)$ in $\mathcal{P}'_i$.

$$
\begin{aligned}
y'_{ij_{k+1}} - y'_{ij_k} &= \Delta \left(j_{k+1} - j_k \right) + \left(\epsilon_{ij_{k+1}} - \epsilon_{ij_k} \right) \\
&= \Delta r + \epsilon_{ij_{k+1,k}},
\end{aligned}
$$

where $r = j_{k+1} - j_k$ and $\left| \epsilon_{ij_{k+1,k}} \right| = \left| \epsilon_{ij_{k+1}} - \epsilon_{ij_k} \right|$ is small. Thus we see that there are $r-1$ missing middle comb pulses between the j_k-th and j_{k+1}-th detected comb pulses in comb i if we can write $y'_{ij_{k+1}} - y'_{ij_k} = \Delta r + \epsilon_{ij_{k+1,k}}$. Solving for r, we have that

$$
r = \frac{y'_{ij_{k+1}} - y'_{ij_k}}{\Delta} - \frac{\epsilon_{ij_{k+1,k}}}{\Delta}. \tag{3}
$$

Hence r can be computed from the data by

$$
r = \text{round} \left(\frac{y'_{ij_{k+1}} - y'_{ij_k}}{\Delta} - \frac{\epsilon_{ij_{k+1,k}}}{\Delta} \right) \approx \text{round} \left(\frac{y'_{ij_{k+1}} - y'_{ij_k}}{\Delta} \right), \tag{4}
$$

where round $(\cdot)$ is the nearest integer function; the approximation is exact provided that the inequality

$$\left| \left\{ \frac{y'_{ij_{k+1}} - y'_{ij_k}}{\Delta} \right\} - \frac{1}{2} \right| > \left| \frac{\epsilon_{ij_{k+1},k}}{\Delta} \right|, \tag{5}$$

holds where $\{x\} = x - \lfloor x \rfloor$ is the fractional part of x. Since $\left| \frac{\epsilon_{ij_{k+1},k}}{\Delta} \right| << 1$, the inequality almost always holds in practice, so equation 4 can be used to calculate the number of missing middle comb pulses from the data.

Since the comb generator is split into ten fibers, it is a reasonable requirement that each comb have the same number of comb pulses. This prompts the following definition.

Definition 7. Suppose that comb i has m_i detected comb pulses and $r - 1$ missing middle comb pulses. Let $M = \max_i m_i$. If $m_i + r - 1 < M$, then comb i has $M - m_i - r + 1$ *missing comb pulses at the end of comb* i.

A general way for characterizing invalid comb pulses is much more difficult. A very heuristic but sometimes unreliable way to identify an invalid comb pulse in comb i is to assume that the difference of the comb pulses' x-coordinate and the average of the comb pulses' x-coordinates in comb i are normally distributed with mean 0 and standard deviation 1. Under this heuristic approach, an invalid comb pulse in comb i is one that is an outlier. Let δ be the difference of the x-coordinate value of a particular comb pulse in comb i and the average of the x-coordinates in comb i. We say that that comb pulse is an outlier if δ is outside the range of $[Q_1 - 3/2 (Q_3 - Q_1), Q_3 + 3/2 (Q_3 - Q_1)]$ where Q_1 and Q_3 are the upper and lower quartile of the standard normal distribution respectively.

3.2 Determining Corresponding Homolog Positions in I

Recall that to create a TPS mapping, we need to define corresponding homolog points $(x_{ij}, y_{ij}) \in I$ for each valid $(x'_{ij}, y'_{ij}) \in I'$. In this section, we present our method of determining the corrected homolog points in I. Let $\mathcal{P}'^{(v)}_i = \left\{ \left(x'_{ij_k^{(v)}}, y'_{ij_k^{(v)}} \right) \mid j_k^{(v)} \in J_i^{(v)} \right\}$ denote the set of valid comb pulses as defined in Definition 5 in comb i in I', where $J_i^{(v)}$ is the index set for the valid comb pulses in comb i. Note that $\mathcal{P}'^{(v)}_i \subset \mathcal{P}'_i$ and $J_i^{(v)} \subset J_i$ for $i = 0, \ldots, 9$. Also let $\mathcal{P}'^{(v)} = \bigcup_{i=0}^{9} \mathcal{P}'^{(v)}$. To avoid confusion, we will associate the superscript (v) with *valid* comb pulses.

The homolog x-coordinates are calculated in a straightforward manner. For each comb i, we set

$$x_{ij} = \frac{\sum_{(x', y') \in \mathcal{P}'^{(v)}_i} x'}{\left| \mathcal{P}'^{(v)}_i \right|} \quad \text{for all} \ \ j \in J_i^{(v)}, \tag{6}$$

where $\left| \mathcal{P}'^{(v)}_i \right|$ is the number of elements in $\mathcal{P}'^{(v)}_i$. In other words, the homolog x-coordinates for comb i is the mean of the x-coordinates of the valid comb pulses in comb i in I'.

Recall from section 3, we assume that $y'_{ij} = b_i + \Delta j + \epsilon_{ij}$ where b_i is the fiber-bundle delay associated with comb i, Δ is the comb frequency in pixels, and $|\epsilon_{ij}| << \Delta$. The quantity ϵ_{ij} represents the small nonlinear shifts in the y-direction (temporal direction). To assign the homolog y-coordinates, we need to choose a valid comb pulse in I' to serve as a reference point. Let

$$\left(x'_{i_r j_r^{(v)}}, y'_{i_r j_r^{(v)}} \right) = \underset{(x', y') \in \mathcal{P}'^{(v)}}{\mathrm{argmin}} \left\| \left(\frac{N}{2}, \frac{N}{2} \right) - (x', y') \right\| \tag{7}$$

be the reference point in I'; that is, $\left(x'_{i_r j_r^{(v)}}, y'_{i_r j_r^{(v)}} \right)$ is the point closest to the center of I. This is based on the belief that the center of the image is usually the least distorted region. For comb i_r, we define the homolog y-coordinates to be

$$y_{i_r k} = y'_{i_r j_r^{(v)}} + \Delta \left(k - j_r^{(v)} \right) \quad \text{for all} \ \ k \in J_{i_r}^{(v)}. \tag{8}$$
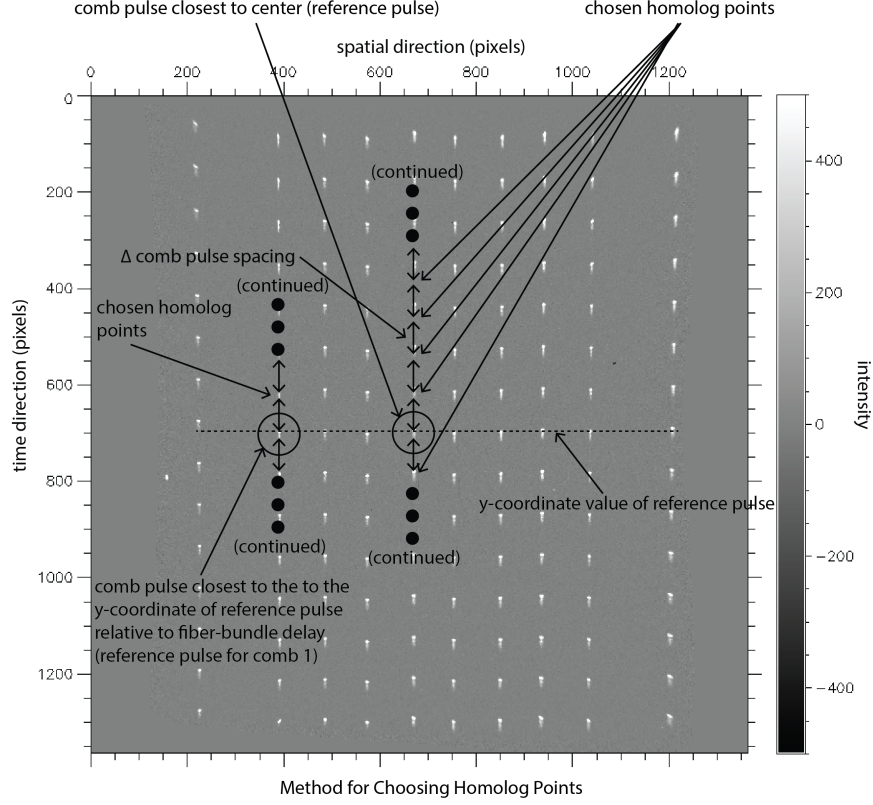
Figure 5. An illustration to demonstrate the method for choosing the homolog points.

For all other combs $i \neq i_r$, we also choose a reference comb pulse to generate the other homolog points. For each comb $i \neq i_r$, let $\left(x'_{ij_{r_i}^{(v)}}, y'_{ij_{r_i}^{(v)}}\right)$ be the valid comb pulse in comb i in I' such that

$$y'_{ij_{r_i}^{(v)}} = \operatorname*{argmin}_{y' \in \left\{\hat{y}' \mid (x', \hat{y}') \in \mathcal{P}_i^{'(v)}\right\}} |\alpha'_i - y'|, \tag{9}$$

where $\alpha'_i = y'_{i_r j_{r}^{(v)}} + (b_i - b_{i_r})$. That is, choose the reference comb pulse in comb i to be the pulse whose y-coordinate is closest to the y-coordinate of the center reference point in I' given by equation 7 relative to the difference in the fiber-bundle delays associated with combs i and i_r. Now the homolog y-coordinate for each comb $i \neq i_r$ is given by

$$y_{ik} = \alpha'_i + \Delta \left(k - j_{r_i}^{(v)}\right) \quad \text{for all} \ \ k \in J_i^{(v)}. \tag{10}$$

Figure 5 illustrates the method for choosing the homolog y-coordinates in I given in equations 8 and 9. At this point we have the valid landmark points $\left(x'_{ij^{(v)}}, y'_{ij^{(v)}}\right) \in I'$ and their homologs $\left(x_{ij^{(v)}}, y_{ij^{(v)}}\right)$ as required by the TPS algorithm. Under the thin-plate splines mapping f, we have the mapping $\left(x'_{ij^{(v)}}, y'_{ij^{(v)}}\right) \overset{f}{\longmapsto} \left(x_{ij^{(v)}}, y_{ij^{(v)}}\right)$ for all $i = 0, ..., 9$ and $j^{(v)} \in J_i^{(v)}$.

3.3 Determining Landmark Boundary Points for I' and I

To prevent the image from resizing, we need to approximate the boundary of I' and enforce the mapping $\partial I' \mapsto \partial I$ under the TPS warp-correction map. Here the notation ∂A means the boundary of the set $A \subset \mathbb{R}^2$. Enforcing the mapping $\partial I' \mapsto \partial I$ in a careful way will ensure that area $(I') = $ area (I). To see that a boundary mapping is necessary, consider the following example.
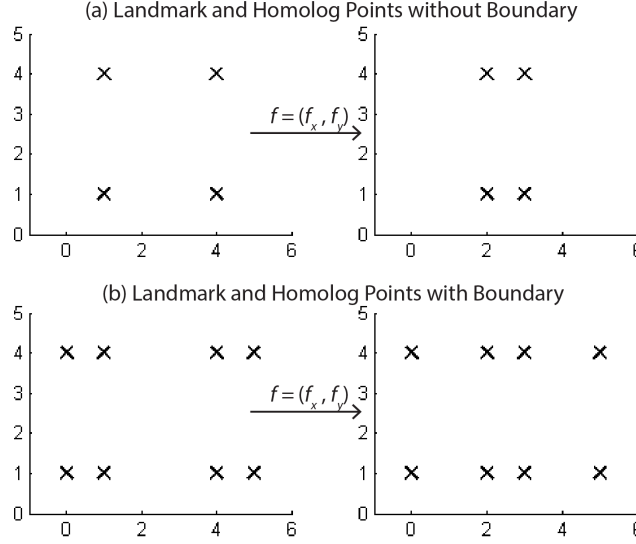
Figure 6. (a) landmark and homolog points not including the boundary; (b) landmark and homolog points including the boundary.

Example 1. Suppose that $I' = [0,5] \times [0,5]$, and let $\{(1,1),(1,4),(4,4),(4,1)\} \subset I'$ be the set of landmark points. Choose the corresponding homolog points to be $\{(2,1),(2,4),(3,4),(3,1)\} \subset I$. We will construct a TPS mapping so that $(1,1) \mapsto (2,1)$, $(1,4) \mapsto (2,4)$, $(4,4) \mapsto (3,4)$, and $(4,1) \mapsto (3,1)$. Notice that each y-coordinate is identically mapped so $f_y(x,y) = y$. See figure 6a. Solving equation 14 in section 8 yields the following mapping for the x-coordinates, $f_x(x,y) = 1.667 + 0.333x + 10^{-16}\big[0.1128U\left(\|(1,1)-(x,y)\|\right) - 0.0954U\left(\|(1,4)-(x,y)\|\right) - 0.1691U\left(\|(4,4)-(x,y)\|\right) + 0.0867U\left(\|(4,1)-(x,y)\|\right)\big]$. We thus have the TPS mapping $f(x,y) = (f_x(x,y), f_y(x,y))$. Notice that $f(0,y) = (1.6667,y))$, and $f(5,y) = (3.3333,y)$. This means that the left and right boundary of I shift by $+1.6667$ and -1.6667 respectively, shrinking the resulting image of I. See figure 7a.

Now consider the same set of landmark and homolog points, but include the boundary landmark points $\{(0,1),(0,4),(5,1),(5,4)\} \subset \partial I'$ and map them identically in I. See figure 6b. The resulting TPS mapping for the x-coordinates is given by

$$f_x(x,y) = -1.2768 + 1.5107x +$$
$$0.1950\big[U\left(\|(1,1)-(x,y)\|\right) + U\left(\|(1,4)-(x,y)\|\right) - U\left(\|(4,4)-(x,y)\|\right) - U\left(\|(4,1)-(x,y)\|\right)\big] -$$
$$0.1170\big[U\left(\|(5,1)-(x,y)\|\right) + U\left(\|(0,4)-(x,y)\|\right) - U\left(\|(5,1)-(x,y)\|\right) - U\left(\|(5,4)-(x,y)\|\right)\big]$$

Again, the y-coordinates are mapped identically. The left and right boundaries of I are given parametrically as $(f_x(0,y),y)$ and $(f_x(5,y),y)$, respectively; see figure 7b. We see from figure 7 that the including landmark boundary points better preserves the area of I.

Since we do not know the exact shape of I', we have to estimate the boundary of I'. To estimate the top and bottom boundaries of I', introduce two functions $g_x(x,y) = a_0 + a_1x + a_2y$ and $g_y(x,y) = b_0 + b_1x + b_2y$. For each comb i, we associate the valid x and y-coordinates of the landmark points in I' with g_x and g_y respectively, and minimize the difference in the least-squares sense to obtain the coefficients for g_x and g_y. More formally, we minimize the function

$$\chi\left(\boldsymbol{\beta}_x, \boldsymbol{\beta}_y\right) = \sum_{j \in J_i^{(v)}} \left[\left(x'_{ij} - g_x\left(x'_{ij}, y'_{ij}; \boldsymbol{\beta}_x\right)\right)^2 + \left(y'_{ij} - g_y\left(x'_{ij}, y'_{ij}; \boldsymbol{\beta}_y\right)\right)^2\right], \tag{11}$$
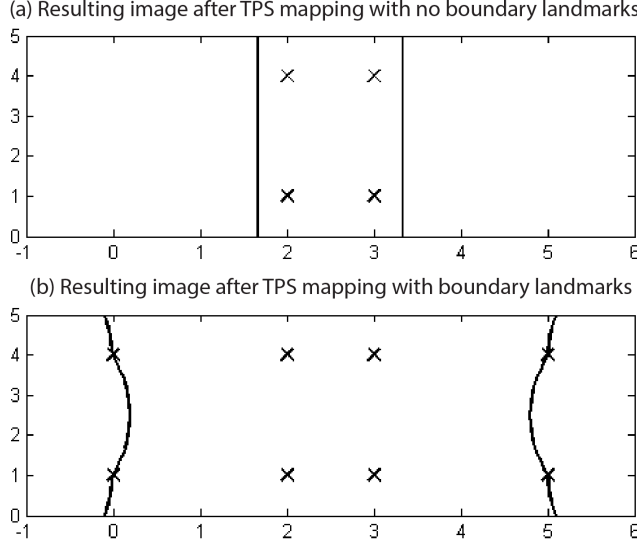
Figure 7. (a) Resulting image after the TPS mapping with no boundary points; and (b) resulting image after TPS mapping with boundary points. We see that the TPS mapping with boundary preserves the area better.

where $\boldsymbol{\beta}_x = (a_0, a_1, a_2)$ and $\boldsymbol{\beta}_y = (b_0, b_1, b_2)$ are the parameter vectors for g_x and g_y respectively. This minimization is done for each comb $i = 0, \ldots, 9$, obtaining 10 different polynomials. The estimated top and bottom landmark boundary points for I' are thus given by $(g_x(x_{ij}, 1364), g_y(x_{ij}, 1364))$ and $(g_x(x_{ij}, 0), g_y(x_{ij}, 0))$ respectively for each comb i and for some $j \in J_i^{(v)}$. Note that the actual choice of $j \in J_i^{(v)}$ is irrelevant since all x_{ij}'s are equal (recall from equation 6 that they are the average the x-coordinates of the valid landmark points in I'). The corresponding homolog points for the top and bottom boundaries of I are given by $(1364, x_{ij})$ and $(0, x_{ij})$ respectively for each comb i and for some $j \in J_i^{(v)}$.

The method for estimating the left and right boundaries is similar except that it is more difficult to write down formally. Let

$$m^{(v)} = \max_{i=0,\ldots,9} J_i^{(v)}$$

That is, $m^{(v)}$ is the largest valid comb pulse index. For each comb i and for each $j = 0, 1, \ldots, m^{(v)} - 1$, construct the set $R_{ij} = \left\{ \left(x'_{ij^{(v)}}, y'_{ij^{(v)}} \right) \mid j^{(v)} = j \text{ and } j^{(v)} \in J_i^{(v)} \right\}$. Let $R_j = \bigcup_{i=0}^{9} R_{ij}$. Informally, R_j is the set of valid comb pulses in the same row. Similarly, to the top and bottom boundary case, we fit the polynomials g_x and g_y to the x and y-coordinates of R_j in the least-squares sense. That is, we minimize the function

$$\chi\left(\boldsymbol{\beta}_x, \boldsymbol{\beta}_y\right) = \sum_{(x',y') \in R_j} \left[\left(x' - g_x\left(x', y'; \boldsymbol{\beta}_x\right) \right)^2 + \left(y' - g_y\left(x', y'; \boldsymbol{\beta}_y\right) \right)^2 \right], \tag{12}$$

for each $j = 0, \ldots, m^{(v)} - 1$. We thus end up with $m^{(v)}$ polynomials, one for each row of valid comb pulses. The estimated left and right boundary landmark points for I' are given by $(g_x(0, \Delta j), g_y(0, \Delta j))$ and $(g_x(1364, \Delta j), g_y(1364, \Delta j))$ respectively for each $j = 0, 1, \ldots, m^{(v)} - 1$, and where Δ is the fiber-bundle delay. The corresponding homolog points for the left and right boundary points in I are given by $(0, \Delta j)$ and $(1364, \Delta j)$ respectively for each $j = 0, 1, \ldots, m^{(v)} - 1$.

The interior landmark and homolog points as well as the boundary landmark and homolog points are used for the generation of the TPS warp-correction mapping.

Shot N130120-001-000_508: Image of Uncorrected Image Subtracted from the Warp-Corrected Image
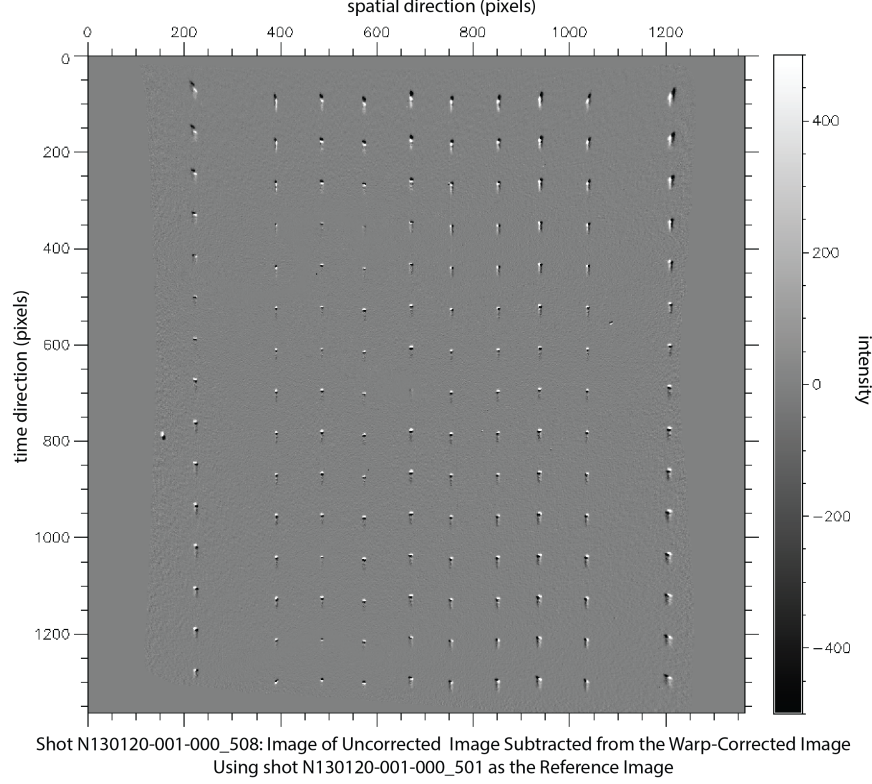Using shot N130120-001-000_501 as the Reference Image

Figure 8. The resulting image from subtracting the uncorrected image from shot N130120-001-000_501 from the corrected image from shot N130120-001-000_501 using the warp-correction map generated from the reference image from shot N130120-001-000_508. Notice that the resulting correction is very small and difficult to see qualitatively.

4. PERFORMANCE OF THE THIN-PLATE SPLINES WARP CORRECTION

In this section, the performance of the thin-plate splines warp-correction algorithm on ten-comb streak camera images with various sweep durations are examined.

The comb frequency is known to 0.01% [8]. The comb frequency thus provides a good baseline to evaluate the performance of the TPS warp correction. We consider shots in which there are multiple ten-comb images available. Suppose that a particular NIF shot X has n ten-comb images $I'_0, I'_1, \ldots, I'_{n-1}$ with a particular comb frequency. We arbitrarily choose one of the n ten-comb images, say image I'_k, which we call the *reference image*. The TPS warp-correction algorithm is then performed on image I'_k, generating the associated warp-correction map f_k. The warp-correction map f_k is then applied to all the other ten-comb images I'_j for $j \neq k$. The comb pulses on the resulting warp-corrected images I_j are measured by a peak-detection algorithm and the frequency is inferred and compared to the known comb frequency.

The comb generator has fundamental jitter in its trigger electronics, and pulses emitted by the comb generator vary randomly in timing with a root mean square of about 15 picoseconds. The VISAR system requires the measurement accuracy to be within one pixel in the temporal direction. Let S be the standard deviation of the difference between the measured comb frequency for ten-comb image I'_j and the known comb frequency. If $S < \max\{1 \text{ pixel}, 15 \text{ picosecond pixel equivalent}\}$, then we say that the warp-correction for I'_j is *successful*.

The warp-corrections are very small and difficult to see qualitatively. Let us examine the results of the TPS warp-correction on ten-comb image shot N130120-001-000_501 (streak camera A) in detail. Figure 8 shows a typical warp-correction using a reference image. For the ten-comb shots in N130120-001-000, the known comb frequency is 0.5 Ghz with a sweep duration of 31.59 ns. Converting nanoseconds to pixels, we have that the comb period for the ten-comb shots in N130120-001-000 is about 86.42 pixels. Measuring the deviation of the measured
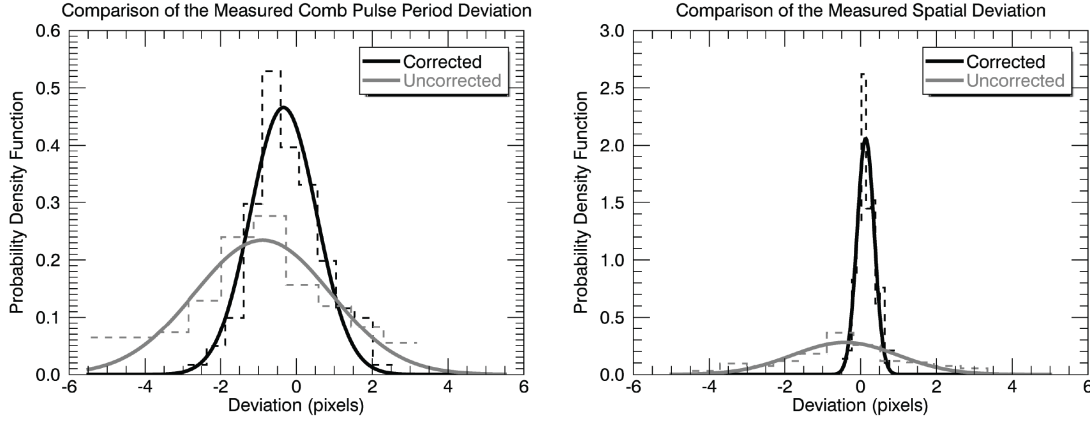
Figure 9. Comparison of the PDFs in the temporal and spatial directions for the uncorrected and corrected images. The histograms used to approximate the PDFs are displayed as the dashed lines.

Table 1. Comparison of the mean and standard deviation for the corrected and uncorrected image for shot N130120-001-000_501 with a sweep duration of 31.586 ns and comb frequency of 0.5 Ghz.

shot N130120-001-000_501 (streak A) ref. *_508				
	temporal (pixels)		spatial (pixels)	
	mean	stddev	mean	stddev
uncorrected	-0.89179	1.7958	-0.40934	1.3886
corrected	-0.18679	0.82125	0.20697	0.26444

comb period to 86.42 and organizing the deviation data into normalized histograms, we get an approximation to the probability density function (PDF) of the measured comb period deviations. The PDF of the measured comb period deviations is assumed to be normal, so we fit a Gaussian function to the normalized histogram to extract the mean and standard deviation. The left graph of figure 9 compares the PDF of the comb period deviation of the uncorrected and corrected images. The mean and standard deviation are displayed in table 1. We see that under the TPS warp correction, we have improvement in both the mean and standard deviation.

The same analysis can be done in the spatial direction, measuring the comb pulse deviations of the pulses in comb i to the average of the x-coordinates of comb i. The right graph of figure 9 shows the resulting probability density functions of the aggregate all the combs for the corrected and uncorrected images of N130120-001-000. The mean and standard deviation are displayed in table 1. Again, we see improvement in both the mean and the standard deviation of the comb pulse deviation from the average of the x-coordinates.

Tables 1-4 summarize the performance of the TPS warp-correction algorithm in the temporal and spatial direction on ten-comb images of various sweep durations and comb frequencies; the sweep duration (nanoseconds) and comb frequency (Ghz) are provided with the tables. We see that for all four shots, the TPS warp-correction algorithm improves the temporal and spatial mean and standard deviation with the exception of shot N130124-002-000_508 listed in table 4. For shot N130124-002-000_508, the mean decreases in both the temporal and spatial directions and the standard deviation decreases for the spatial direction; but, the standard deviation increases in the temporal direction. However, this is still a successful warp correction since the standard deviation is below the pixel equivalent of 15 picoseconds.

5. SUMMARY AND CONCLUDING REMARKS

VISAR is the primary diagnostic used for measuring the timing of shocks—one of the key performance metrics for the NIF's performance to achieve ignition. Correcting for the nonlinear temporal and spatial distortions present in the diagnostics three streak cameras are essential for accurately measuring the shock timing. A detailed

Table 2. Comparison of the mean and standard deviation for the corrected and uncorrected image for shot N130120-001-000_502 with a sweep duration of 31.586 ns and comb frequency of 0.5 Ghz.

shot N130120-001-000_502 (streak A) ref. *_508				
	temporal (pixels)		spatial (pixels)	
	mean	stddev	mean	stddev
uncorrected	-0.89179	1.7959	-0.40934	1.3886
corrected	-0.34115	0.86976	0.13326	0.22522

Table 3. Comparison of the mean and standard deviation for the corrected and uncorrected image for shot N140123-004-000_514 with a sweep duration of 45.45 ns and comb frequency of 1 Ghz.

shot N140123-004-000_514 (streak B) ref. *_506				
	temporal (pixels)		spatial (pixels)	
	mean	stddev	mean	stddev
uncorrected	-0.26731	0.45082	-0.35006	1.0760
corrected	-0.09050	0.36832	0.08430	0.16976

calibration procedure developed with NSTec has been applied to the production camera correction analysis for over eight years. However, since the streak camera nonlinearities drift over time due to sweep date jitter and slow thermal drift, an additional in-situ warp correction is needed to measure the shock timing to within the required resolution.

In this paper, a robust in-situ warp correction algorithm was developed utilizing thin-plate splines. Thin-plate splines provide a smooth functional correction that models complex local distortions over scattered and irregularly sampled points—properties needed in an in-situ warp correction for VISAR. The algorithm was made robust by accounting for invalid and missing comb pulses and estimating the image boundary points. We demonstrated improved timing and spatial accuracy for four shots with various sweep durations and comb frequencies. The preliminary results are promising. Future work will involve gathering detailed statistics on the performance of the TPS warp-correction algorithm when applied to ten-comb images of various sweep durations and comb frequencies; and determining a more reliable way to characterize invalid comb pulses.

6. ACKNOWLEDGMENTS

7. APPENDIX A

Basic definitions from real analysis that are used in this paper are presented here for convenience.

Definition 8. Let $X \subset \mathbb{R}^2$. A *path* in X is a mapping $f : [a, b] \to X$ such that f is continuous.

Table 4. Comparison of the mean and standard deviation for the corrected and uncorrected image for shot N130124-002-000_508 with a sweep duration of 11.05 ns and comb frequency of 1 Ghz.

shot N130124-002-000_508 (streak B) ref. *_501				
	temporal (pixels)		spatial (pixels)	
	mean	stddev	mean	stddev
uncorrected	-1.3182	1.0495	-50226	1.2724
corrected	-0.50226	1.2724	-0.35902	0.53561

Definition 9. A space X is *path-connected* if for any two points $x, y \in X$, there exist a path from x to y; more precisely, if there exist a continuous function $f : [a, b] \to X$ such that $f(a) = x$ and $f(b) = y$.

Definition 10. Let S^1 and D^2 denote the unit circle and unit disk in $\mathbb{R}^2$ respectively. A space X is *simply-connected* if it is path-connected and for any continuous map $f : S^1 \to X$, there exist a continuous map $g : D^2 \to X$ such that $g|_{S^1} = f$; i.e., the restriction of g to S^1 is f. In other words, X is simply connected if there are no "holes"; i.e., we can always contract a closed loop to a single point in a continuous fashion without leaving X.

Definition 11. Let $A \subset \mathbb{R}^2$. The interior of A, denoted $\mathrm{int}A$, is the set of all points $x \in A$ such that there exist an open neighborhood $N \subset X$ containing x.

Definition 12. Let $A \subset \mathbb{R}^2$ such that A is closed. The *boundary of A*, denoted ∂A, is defined to be the set-theoretic difference between A and $\mathrm{int}A$; that is, $\partial A = A \backslash \mathrm{int}A$.

Definition 13. Let $A, B \subset \mathbb{R}^2$. A *homeomorphism* is a continuous bijective map $f : A \to B$ whose inverse is also continuous. The map f is a *diffeomorphism* if it and its inverse are differentiable on $\mathrm{int}A$ and $\mathrm{int}B$ respectively.

8. APPENDIX B

In this section, we present a method for finding the coefficients of the component functions f_x and f_y in the thin-plate splines mapping $f(x, y) = (f_x(x, y), f_y(x, y))$. A relationship that is useful for calculating the bending energy (equation 1) is also presented.

The following algebra is presented in Bookstein's paper [10]. Suppose that we have n landmark points $\{(x'_k, y'_k) \mid k = 1, \ldots n\}$ and n homolog points $\{(x_k, y_k) \mid k = 1, \ldots n\}$. In order for the integrand in equation (1) to be integrable, we require that

$$\sum_{k=1}^{n} w_k = \sum_{k=1}^{n} w_k x'_k = \sum_{k=1}^{n} w_k y'_k = 0. \tag{13}$$

Let $\mathrm{Mat}(\mathbb{R}, n, m)$ denote the vector space of matrices with entries in $\mathbb{R}$ and dimensions $n \times m$ (n rows, m columns). Construct the following matrices:

$$
\begin{aligned}
K &\in \mathrm{Mat}(\mathbb{R}, n, n), &&(K)_{ij} = U\left(\left\|(x'_i, y'_i) - (x'_j, y'_j)\right\|\right) \\
P &\in \mathrm{Mat}(\mathbb{R}, n, 3), &&(P)_{ij} = (1, x'_i, y'_i) \\
S &\in \mathrm{Mat}(\mathbb{R}, n, 2), &&(S)_{ij} = (x_i, y_i) \\
O &\in \mathrm{Mat}(\mathbb{R}, 3, 3), &&(O)_{ij} = (0) \\
W &\in \mathrm{Mat}(\mathbb{R}, n, 2), &&W = \left((w_{x_1}, \ldots, w_{x_n})^T, (w_{y_1}, \ldots, w_{y_n})^T\right) \\
A &\in \mathrm{Mat}(\mathbb{R}, 3, 2), &&A = \left((a_{x_1}, a_{x_2}, a_{x_3})^T, (a_{y_1}, a_{y_2}, a_{y_3})^T\right) \\
\hat{O} &\in \mathrm{Mat}(\mathbb{R}, 3, 2), &&(\hat{O})_{ij} = (0)
\end{aligned}
$$

Where T denotes the matrix transpose operator; and $U(r) = r^2 \log r$, $r = \sqrt{x^2 + y^2}$, and $\|\cdot\|$ denotes the standard Euclidean metric. Requiring that $f(x'_k, y'_k) = (x_k, y_k)$ so that each landmark point is mapped to its homolog and the conditions in equation (13), yield the following linear system.

$$\begin{pmatrix} K & P \\ P^T & O \end{pmatrix} \begin{pmatrix} W \\ A \end{pmatrix} = \begin{pmatrix} S \\ \hat{O} \end{pmatrix} \tag{14}$$

Solving this linear system, gives the coefficients for the affine and fully nonlinear parts of the interpolating surfaces $f_x(x, y)$ and $f_y(x, y)$ in (2). Let L be the $(n + 3) \times (n + 3)$ matrix in the system, and let L_n denote the upper-left $n \times n$ sub-block of L. It can be shown that

$$I(f) \propto V^T L_n^{-1} V = W^T K W \tag{15}$$

The proportional relationship is shown in [13].

REFERENCES

[1] Moses, E. I., "Ignition on the National Ignition Facility: a path towards inertial fusion energy," *J. Nucl. Fusion* **49**(104022), 9pp (2009).

[2] Liebman, J., Bond, E., Warrick, A., Azevedo, S., and Chandrasekaran, H., "NIF target diagnostic automated analysis recent accomplishments, turning raw data into performance metrics," (2013). presentation to the 16th Annual Signal and Imaging Sciences Workshop.

[3] Celliers, P. M., Collins, G. W., Da Silva, L. B., Gold, D. M., Cauble, R., Wallace, R. J., Foord, M. E., and Hammel, B. A., "Shock-induced transformation of liquid deuterium into a metallic fluid," *Phys. Rev. Lett.* **84**(24), 5564–5567 (2000).

[4] Munro, D. H., Celliers, P. M., Collins, G. W., Gold, D. M., Da Silva, L. B., Haan, S. W., Cauble, R. C., Hammel, B. A., and Hsing, W. W., "Shock timing technique for the National Ignition Facility," *Physics of Plasmas* **8**, 2245 (2001).

[5] Malone, R. M., Frogget, B. C., Kaufman, M. I., Tunnell, T. W., Guyton, R. L., Reinbachs, I. P., Watts, P. W., Celeste., J. R., Celliers, P. M., Lee, T. L., MacGowan, B. J., Ng, E. W., Robinson, R. B., and Seppala, L. G., "Overview of the line-imaging VISAR diagnostic at the National Ignition Facility (NIF)," in [*International Optical Design Conference 2006*], **6342**, SPIE (July 2006).

[6] Silbernagel, C. T., Torres, III, P., and Kalantar, D. H., "A method for analyzing high resolution, time domain, streak camera calibration data," in [*Advanced Signal Processing Algorithms, Architectures, and Implementations XIV*], **5559**, SPIE (August 2004).

[7] Charest, Jr., M. R., Torres, III, P., Silbernagel, C. T., and Kalantar, D. H., "Reliable and repeatable characterization of optical streak cameras," *Rev. Sci. Instrum.* **79** (2008).

[8] Datte, P., Celliers, P. M., Kalantar, D. H., Moody, J., Bond, E., Hibbard, R., Krauter, K., Nelson, J., and Warrick, A., "Operational experience with optical streak cameras at the National Ignition Facility," in [*Target Diagnostics Physics and Engineering for Inertial Confinement Fusion II*], **8850**, SPIE (September 2013).

[9] Erikson, A. P. and Åström, K., "On the bijectivity of thin-plate splines," in [*Analysis for Science, Engineering and Beyond*], Åström, K., Persson, L., and Silvestrov, S. D., eds., *Springer Proceedings in Mathematics* **6**, 93–141, Springer Berlin Heidelberg (2012).

[10] Bookstein, F. L., "Principal warps: Thin-plate splines and the decomposition of deformations," *IEEE Transactions on Pattern Analysis and Machine Intelligence* **11**(6), 567–585 (1989).

[11] Duchon, J., "Interpolation des fonctions de deux variables suivant le principe de la flexion des plaques minces," *RAIRO Analyse Numérique* **10**, 5–12 (1976).

[12] Meinguet, J., "Multivariate interpolation at arbitrary points made simple," *Zeitschrift für Angewandte Mathematik und Physik (ZAMP)* **30**, 292–304 (1979).

[13] Powell, M., "A thin plate spline method for mapping curves into curves in two dimensions," in [*Computational Techniques and Applications: CTAC95*], 43–57, World Scientific (1995).